PCCP

Cite this: *Phys. Chem. Chem. Phys.*, 2012, **14**, 6826–6832

www.rsc.org/pccp

PAPER

Comparison of scattering and reflection SFG: a question of phase-matching

Hilton B. de Aguiar,[ab] Rüdiger Scheu,[ab] Kailash C. Jena,[ab] Alex G. F. de Beer[b] and Sylvie Roke*[ab]

Received 2nd February 2012, Accepted 20th March 2012
DOI: 10.1039/c2cp40324b

We present a comparison between sum frequency scattering (SFS) and reflection mode sum frequency generation (R-SFG). We have used scattering theory to describe both scattering experiments as well as reflection mode experiments. The interfacial vibrational spectrum of nanoscopic oil droplets dispersed in water was probed with SFS as well as with R-SFG. Spectra recorded in phase-matched R-SFG mode and spectra recorded with SFS from the same sample are different, which shows that different interfaces are measured. Scattering spectra at different scattering angles agree with nonlinear light scattering theory. We further present experiments with polymer films aimed at quantifying the comparative strength of R-SFG and SFS experiments.

Introduction

Molecular surface properties, such as composition, orientation, and chirality, can be probed using second-order nonlinear optical methods.[1,2] In such experiments the second-order susceptibility is probed, which contains information on the surface averaged molecular hyperpolarizability and molecular orientation. Measurements can be performed using pulsed laser beams that contain identical frequency components (Second Harmonic Generation, SHG[3–6]), or using two pulsed laser beams with non-identical frequency components (Sum Frequency Generation, SFG[7–13]). When one of the beams contains frequency components in the infrared (IR), which are resonant with vibrational transitions in the surface layer, while the other beam is composed of frequency components that are off-resonance, then the vibrational spectrum of a surface layer can be probed. This vibrational response consists therefore of a combined IR and Raman transition. Such a combined transition generally only occurs (within the electric dipole approximation) in regions with absence of centrosymmetry. The absence of centrosymmetry either occurs in non-centrosymmetric materials or at interfaces between centrosymmetric media.

SHG and SFG experiments can be performed in reflection, transmission and scattering geometry. In transmission experiments performed in a non-centrosymmetric crystal the laws of momentum and energy conservation demand that the following relationships hold between the $\boldsymbol{k}$-vectors of the involved beams: $\boldsymbol{k}_1 + \boldsymbol{k}_2 = \boldsymbol{k}_0^0$ (ref. 1) and $\omega_0 = \omega_1 + \omega_2$ for the frequencies of the beams. The index for $\boldsymbol{k}$ and ω signifies the center frequency of the beams, and the lowest index corresponds to the highest center frequency. This set of equations is known as the phase matching condition. In a reflection mode experiment, momentum conservation is required parallel to the surface so that $\boldsymbol{k}_{1,\parallel} + \boldsymbol{k}_{2,\parallel} = \boldsymbol{k}_{0,\parallel}^0$. This determines the direction in which the reflected SFG photons are emitted.

In Second Harmonic Scattering (SHS),[14,15] and Sum Frequency Scattering (SFS) experiments[12,16] the interfaces of nanoscopic objects such as particles,[14,17–24] droplets[25–29] and vesicles[30–32] can be probed. In such experiments the beams are passing through a sample that consists of multiple particles that are smaller than the wavelength of the emitted light, so that there is no reflection but rather refraction and this seemingly opposes the condition of phase-matching.

Here, we will treat some of the differences between reflection and transmission SFG experiments on the one hand and scattering SF experiments on the other. The results can apply equally to SHG/SHS. First, we will discuss the underlying physics that is needed to explain the SFS process and show that there is no violation of the phase-matching condition, rather the finite particle size results in an unfulfilled phase-matching. We then consider what the consequences are in terms of signal strength by performing R-SFG and SFS measurements on the same sample, a dispersion of oil droplets in water, stabilized with the sodium dodecylsulfate (SDS) surfactant contained in a CaF_2 sample cell. We can therefore probe both the CaF_2–SDS–D_2O sample cell–solution interface as well as the oil droplet–SDS–D_2O interface. Both methods generate spectra, with a different spectral shape, indicating that the chemical environments of SDS at the interface of the CaF_2–solution and the interface of the nanoscopic droplet are different. To further characterize the scattering process we measured scattering spectra at different scattering angles. The results agree with nonlinear light scattering theory. Finally, we have performed experiments with non-centrosymmetric crystalline polymer films in contact with a droplet dispersion.

[a] *Laboratory for fundamental BioPhotonics (LBP), Institute of Bio-engineering (IBI), School of Engineering (STI), École Polytechnique Fédérale de Lausanne (EPFL), CH-1015 Lausanne, Switzerland. E-mail: sylvie.roke@epfl.ch*
[b] *Max-Planck-Institute for Intelligent Systems, Heisenbergstrasse 3, 70569 Stuttgart, Germany*

SFS and the phase-matching condition

In the SFS experiments performed here, IR and VIS beams pass through a dispersion of oil droplets in water. A sketch of the beam geometry is presented in Fig. 1A. The beams induce a second-order nonlinear optical response that is usually described in terms of a nonlinear polarization. For a second-order process that occurs on the droplet surface, the coupling of two incoming electric fields with the surface susceptibility $\boldsymbol{\chi}^{(2)}$ generates the second-order polarization $\boldsymbol{P}_0^{(2)}$, given by

$$\boldsymbol{P}_0^{(2)} = \boldsymbol{\chi}^{(2)}:\boldsymbol{E}_1\boldsymbol{E}_2 \qquad (1)$$

We assume that the fields are plane waves of the form $\boldsymbol{E}_n = E_n\boldsymbol{u}_n e^{i\boldsymbol{k}_n\cdot\boldsymbol{r}}$, where subscripts $n = 0, 1, 2$ denote the participating waves in decreasing order of photon energy, starting at 0 for the (scattered) sum frequency field. The scattered sum frequency wave vector is denoted as $\boldsymbol{k}_0$ and the sum of the wave vectors $\boldsymbol{k}_1$ and $\boldsymbol{k}_2$ is indicated as $\boldsymbol{k}_0^0$. E_n is the field amplitude, $\boldsymbol{u}_n$ is the unit polarization vector and $\boldsymbol{k}_n$ is the wave vector of the corresponding wave n. The polarization components are defined as p for horizontal (in-plane) polarized light, and s for vertical (out of plane) polarized light. Three letter combinations start with the highest frequency term and end with the lowest frequency term. For all fields and polarizations an implicit time dependence $e^{-i\omega_n t}$ is assumed, with ω_n being the oscillation frequency. Important for the description of scattering is the scattering vector $\boldsymbol{q}$ which is defined as $\boldsymbol{k}_0 - \boldsymbol{k}_0^0$.

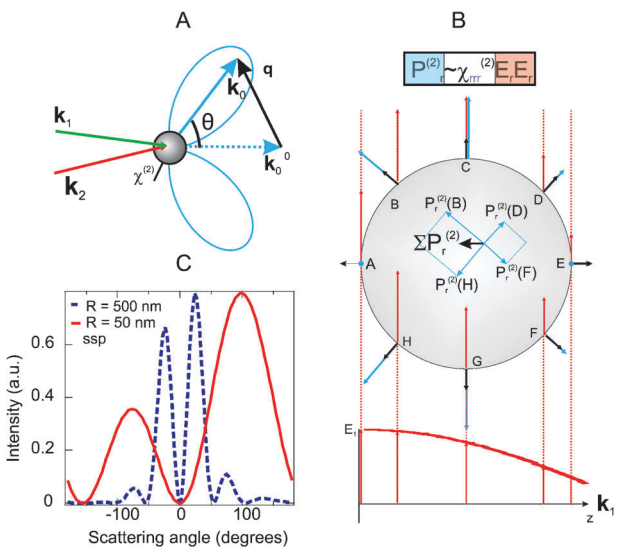

Fig. 1 (A) Illustration of the scattering geometry. (B) Illustration of the effect of relative size. A single beam ($\boldsymbol{E}_1$, $\boldsymbol{k}_1$, bottom of the figure) interacts with a sphere with a surface susceptibility $\chi^{(2)}_{rrr} \neq 0$ (indicated as radially directed arrows with equal length). As the sphere and the wavelength are comparable, different polarization components are created on different points on the surface (indicated as radially directed arrows with variable length). The sum polarization of the printed 8 points oscillates along the direction of the incoming wave vector. (C) Scattering patterns for ssp polarization, for C_{3v} groups with a molecular tilt angle of 30° with respect to the local surface normal (*i.e.* the radial direction) for $R = 500$ nm and $R = 50$ nm. Other parameters: IR/VIS opening angle: 30°, IR wavelength 3447 nm, VIS wavelength 800 nm, $\beta_{aac}/\beta_{ccc} = 3$, $\beta_{aca} = \beta_{caa} = 0$. The patterns are normalized. The NLS-Simulate program was used.[33]

Basic understanding can be achieved by considering a spherical particle or a droplet with only a few surface dipoles and a single $\boldsymbol{\chi}^{(2)}$ component. On such a spherical droplet with a radius R that is of the same order of magnitude or smaller than the wavelength of the emitted sum frequency field, the phase and amplitude of the induced polarization depend on the position on the droplet. Fig. 1B illustrates this effect of relative size. Here, the generated second-order polarization components in the radial direction are drawn for eight points on a sphere. The size of the sphere is comparable to the wavelength of the incident beam. For simplicity we use single beam illumination (*i.e.* SHS case) and a single non-vanishing $\boldsymbol{\chi}^{(2)}$ component ($\chi^{(2)}_{rrr}$). As the amplitude of the wave changes when it moves through the particle, the generated polarization has a different phase at different points on the surface. To consider the emission pattern of one particle, the polarization components need to be summed up. Doing this for the 8 points in Fig. 1B, the remaining polarization oscillates in the z-direction parallel to the incoming field. An oscillating dipole does not emit in the forward direction. Instead, scattered light will appear with maximum intensity at a 90° scattering angle.

To compare how phase-matching enters in both scattering and reflection SFG we can take a closer look at the effective susceptibility. The angle-dependent effective particle susceptibility $\boldsymbol{\Gamma}^{(2)}$ represents the nonlinear response of a scatterer for a given beam geometry. The relation between the effective susceptibility and the interacting electromagnetic waves is given by:

$$E_0 \propto E_1E_2\boldsymbol{u}_0\cdot\boldsymbol{\Gamma}^{(2)}(\boldsymbol{\chi}^{(2)},R,\theta):\boldsymbol{u}_1\boldsymbol{u}_2, \qquad (2)$$

where R is the particle or droplet radius and θ the scattering angle. The components of $\boldsymbol{\Gamma}^{(2)}$ reflect the *combined* symmetry of the scatterer and interacting electromagnetic fields[12] and are given by:

$$\Gamma^{(2)}_{jkl} \propto \int_V \boldsymbol{e}_j\cdot\boldsymbol{\chi}^{(2)}:\boldsymbol{e}_k\boldsymbol{e}_l e^{i\boldsymbol{q}\cdot\boldsymbol{r}'}\mathrm{d}V, \qquad (3)$$

where $\boldsymbol{e}_{j,k,l}$ are the unit vectors spanning the Cartesian coordinate frame of $\Gamma^{(2)}$. Note that in eqn (2) and (3) we have made use of a contracted notation: the contraction in eqn (2) should include the inner product of the laboratory frame with the scattering frame, and the contraction in eqn (3) should contain inner products of the scattering frame with the local coordinate system of the droplet. For the remainder of the text these inner products are not relevant. Integration of eqn (3) is carried out over the enclosed volume V of the particle. For surface scattering we take for the susceptibility $\boldsymbol{\chi}^{(2)} = \boldsymbol{\chi}^{(2)}_s\delta(\boldsymbol{r}' - R)$, where the components are defined relative to the surface normal. The value of the contraction $\boldsymbol{e}\cdot\boldsymbol{\chi}^{(2)}:\boldsymbol{e}\boldsymbol{e}$ varies with the position on the surface.

To consider scattering from a droplet, we need to integrate over the volume of the particle, so that the actual response will depend on the size and shape of the object, which is embedded in $\boldsymbol{\Gamma}^{(2)}$. For a sphere with a non-chiral surface response $\boldsymbol{\Gamma}^{(2)}$ is described as a summation of $\boldsymbol{\chi}^{(2)}$ components that are weighted by form factor functions for a spherical particle (see *e.g.* ref. 33). For a chiral surface the form factors are different.[34] Fig. 1C shows a graph of a calculated scattering pattern for droplets with radii of 50 and 500 nm. The exact calculation was performed using the method and freeware of ref. 33. The polarization combinations that appear from an

SFS experiment are determined both by the surface structure and by the shape of the particle. For small particles and particles with a small contrast between the dielectric constants of the bulk and droplet medium, no emission occurs in the phase-matched direction ($\boldsymbol{k}_0^0 = \boldsymbol{k}_1 + \boldsymbol{k}_2$, *i.e.* $\theta = 0^\circ$, or $q = 0$).

Seemingly in contrast to SFS measurements, R-SFG or transmission mode SFG processes occur exclusively in the phase-matching direction ($\boldsymbol{k}_0^0 = \boldsymbol{k}_1 + \boldsymbol{k}_2$ for transmission or $\boldsymbol{k}_{0,\parallel}^0 = \boldsymbol{k}_{2,\parallel} + \boldsymbol{k}_{1,\parallel}$ for reflection). The polarization dependence is determined by the molecular surface structure at the interface, which follows a different dependence on the surface structure than for SF scattering. The spectrum is determined solely by the molecular conformation and local dielectric environment.

There is, however, no contradiction between the description of the two methods. This can be seen by describing a flat surface response using the equations of the SFS process. If we consider eqn (3) and replace the particle by a flat surface (with surface coordinates $\boldsymbol{r}' = (x', y', 0)$) we will see there is no contradiction. If we take instead of $\boldsymbol{\chi}^{(2)} = \boldsymbol{\chi}_s^{(2)}\,\delta(\boldsymbol{r}' - R)$ for a spherical particle, $\boldsymbol{\chi}^{(2)} = \boldsymbol{\chi}_s^{(2)}\delta(\boldsymbol{z}')$ for a planar surface, we get:

$$\Gamma_{jkl}^{(2)} = \int_{-\infty}^{\infty} \boldsymbol{e}_j \cdot \boldsymbol{\chi}_s^{(2)}\delta(z') : \boldsymbol{e}_k\boldsymbol{e}_l e^{i\boldsymbol{q}\cdot\boldsymbol{r}} d\boldsymbol{r}' = \delta(\boldsymbol{q}_\parallel)\boldsymbol{e}_j \cdot \boldsymbol{\chi}_s^{(2)} : \boldsymbol{e}_k\boldsymbol{e}_l. \tag{4}$$

The result (for illumination of an infinitely large spot size) is emission in the direction of $\boldsymbol{q}_\parallel = \boldsymbol{k}_{0,\parallel}^0 - (\boldsymbol{k}_{2,\parallel} + \boldsymbol{k}_{1,\parallel}) = 0$, *i.e.* in the phase-matched direction only. If the spot size is finite a sinc function peaked in the phase matched direction will be the result. Thus, scattering and phase-matching are two outcomes of the same physical principle. Since the object size compared to the wavelength for scattering is small, and for a phase-matched process it is large, we could say that in the case of SFS and SHS the process of phase-matching is unfulfilled.

Difference between R-SFG *vs.* SFS

Comparing scattering and transmission mode/reflection mode experiments, there are several differences that have to do both with the dimension of the object, as well as the consequential difference in the degree of phase-matching. They are summed up here:

- Small objects have large surface to volume ratios. The total surface area that is probed in a single scattering experiment can be orders of magnitude larger than that in a planar reflection mode experiment. This can result in higher detection sensitivity. As another result of the large surface to volume ratio, the effect of chemical impurities in the bulk phases diminishes greatly, since the surface to volume ratio of small particles can be orders of magnitude larger. For surface studies in planar geometry, impurities in the used chemicals can have a dramatic influence on the outcome of the experiment, even when the purest chemicals are used.[35,36] Additionally, extensive cleaning procedures are often needed to keep the surface clean, which is not necessary in a scattering experiment.
- In SFS or SHS samples can be studied in the medium in which they were prepared, without the need to transfer them to a surface. Reflection mode experiments can also be performed on particles (such as *e.g.* described in ref. 37–42), however, the need to transfer the particles to a substrate could result in an unverifiable change in surface chemistry.
- For SHS and SFS the scattering angle offers an additional experimental parameter. This allows one to optimize conditions for chiral detection,[34] separate charge and surface structure,[43] or selectively measure the interface of objects with different size in the same sample.[44]
- The selection rules for scattering are comparable but vary in terms of the direction in which light will be emitted. Symmetry of $\boldsymbol{\chi}^{(2)}$ will be contained also in $\boldsymbol{\Gamma}^{(2)}$, so that when certain $\boldsymbol{\chi}^{(2)}$ elements are allowed they will give rise to the same $\boldsymbol{\Gamma}^{(2)}$ components. Since the particle geometry determines the weight of each $\boldsymbol{\chi}^{(2)}$ component, the intensity ratios of $\boldsymbol{\Gamma}^{(2)}$ elements are not necessarily equal to that of $\boldsymbol{\chi}^{(2)}$. It can be, but only for a certain value of the product qR.[34]
- Molecular orientation can be retrieved from scattering experiments by measuring the angular dependence, as was done for malachite green on polystyrene beads by Jen *et al.*,[45] and Wunderlich *et al.*[24] or for stearyl chains on silica particles.[16] It can also be achieved by measuring relative polarization combinations, or a combination of both.[21]
- In SHS and SFS experiments scattering processes of different order will have different scattering patterns.[34]
- As scattering experiments are usually performed from uncorrelated objects with no precise phase relationship, a phase sensitive or heterodyne detection scheme cannot be employed. Phase sensitive measurements for SHG and SFG in reflection mode were reported by Chang *et al.* in 1965[46] and Superfine *et al.* in 1990 respectively,[47] and can be used to retrieve the imaginary and real components of $\boldsymbol{\chi}^{(2)}$. Phase sensitive SFG offers the advantage that the complex amplitudes of the real and imaginary parts can be measured with respect to a known reference sample.[48–52] Such a reference comparison is under most scattering conditions not possible, unless a single particle is measured at a fixed position or known trajectory. A particle crystal consisting of single particles (*e.g.* a photonic crystal) would also be usable in a phase sensitive detection scheme. For most scattering applications the relative phase of the imaginary and real components of $\boldsymbol{\Gamma}^{(2)}$ and thus $\boldsymbol{\chi}^{(2)}$ can be retrieved using phase retrieval analysis based on the Maximum Entropy Method (MEM).[53–56] For R-SFG data a comparison has been published with phase sensitive detection and MEM analysis on the same data set,[56] and if appropriate boundary conditions are applied MEM analysis can be used to retrieve the imaginary and real parts of $\boldsymbol{\chi}^{(2)}$.

Possible competing processes

There are two types of interfaces in a dispersion: the droplet interfaces and the interface of the dispersion with the air, or in this case, the sample cell window. Since both interfaces have a nonzero surface susceptibility they can both generate SF photons in the presence of time overlapped IR and VIS beams. There is coherent interaction of the electric field components on the surface of the droplet but no phase-matching. The SF photons from the SF scattering process are generated *inside* the liquid phase and appear with a typical scattering pattern characteristic of which is the absence of scattered light in the forward direction. SF photons generated in a sum frequency

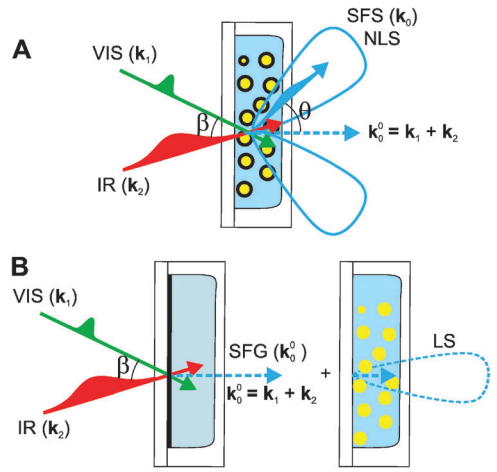

Fig. 2 Two possible sum frequency generation processes that are used in this study. (A) The non-phase-matched SFS process where IR and VIS beams overlap inside a cuvette. The SFS signal is detected at an angle θ, and has a scattering pattern illustrated by the straight line. The SFS process is generated at the droplet–solution interface, illustrated by the thick lines around the droplets. (B) Phase-matched SFG process from the solution–window interface: the SFG signal is generated at the window–solution interface in the phase matched direction (*i.e.*, at $\theta = 0°$). This SF light is then scattered linearly by the droplets in a wide angular range that peaks in the forward direction. The scattering pattern of the linear scattering process is illustrated by the dashed lines.

scattering process will have a certain polarization dependence and an angular scattering pattern. The frequencies that appear in the spectrum are originating from the specific chemical structure at the droplet interface. For the case of light scattering from small particles for which the Rayleigh Gans Debye criteria are satisfied[34] the local dielectric environment does not influence the spectrum. The polarization ratio of the spectra recorded using IR and VIS beams with different polarizations dependence depends on the droplet size and surface structure.[16,33] R-SFG from the window of a sample cell will be emitted in the phase-matched direction. This light can either be reflected or transmitted. When it is transmitted it will undergo linear scattering (LS) through the turbid medium. Linear scattering is peaked in the forward direction. Both processes are illustrated in Fig. 2A (SFS) and Fig. 2B (R-SFG + LS).

Thus, there are fundamental differences between SF scattering and SFG in transmission mode from the window–solution interface. Based on the above description, differences are expected in polarization combination, spectral shape, and angular intensity distribution. Although both processes do not occur at the same location, there may be scenarios in which both processes can contribute to the detected signal. This will be the final topic of this article.

Experimental methods

Emulsions were prepared by adding 1 vol% of perdeuterated hexadecane (d-C16) to a solution of 8 mM SDS in D_2O in a 4 ml vial. We used a two step mixing process, partially following ref. 57. First, mixing was done for 5 min using a hand-held homogenizer (TH, OMNI International). This produced an emulsion with droplets in the micrometer size range which creams in a few minutes. To reduce the creaming rate, the droplet size was decreased further by placing the vial containing the emulsion in an ultrasonic bath (35 kHz, 400 W, Bandelin) for 15 min. The resulting droplets had a radius in the range of ~80–130 nm, which varied per preparation cycle. The polydispersity (PDI) index was below 0.2. The creaming rate for such droplets is 1.3 μm h^{-1}.

Chemicals were used as received: d_{34}-hexadecane (*d*-C16) (98% D) was obtained from Cambridge Isotope. Aqueous solutions were prepared with D_2O (99% D, Aldrich) and sodium dodecylsulfate (SDS) (≥ 99%, Alfa Aesar). The PDLA films were prepared by drop-casting from a 2.5 wt% solutions of polymer powder (D-PLA, Purac Biochem) dissolved in chloroform (>99% Merck). Glassware was cleaned with 3 : 7 H_2O_2 : H_2SO_4 piranha solution and then thoroughly rinsed with ultra pure water (0.053 μS cm^{-1}, TKA) to remove residual chemicals.

The SF experiments are performed using IR pulses (8–12 μJ, ~150 fs, FWHM bandwidth 120 cm^{-1}) spatially and temporally overlapped with 800 nm VIS pulses (8–15 μJ, FWHM bandwidth 5–13 cm^{-1}) in a cuvette containing the emulsion (see ref. 58 for details on the laser system). A 90° off-axis parabolic Au mirror (f = 5 cm) focuses the IR beam down to a ~150 μm beam waist diameter. Two BaF_2 wire grid polarizers were used to control the energy and polarization of the IR beam. The VIS beam polarization is cleaned by a polarizer cube and changed by a $\lambda/2$ plate. The VIS beam was gently focused with a bi-convex lens (f = 50 cm). At the overlapping position, the VIS beam diameter was 240 μm. The angle between VIS and IR beams was set to 15° in a nearly collinear geometry. The cuvettes (Hellma GmbH, 106 O.20–40, Germany) with various optical path lengths consisted of two detachable windows with one side made out of CaF_2 and the other side made out of quartz. The SF scattered beam was collimated with a 0.5″ diameter plano-convex lens (f = 18 mm, Thorlabs), and directed towards the detection system using two 2″ Ag mirrors. The lens was placed at a scattering angle of 60° with the cuvette exit window (quartz side) oriented parallel to the collimating lens. The polarization of the SF signal was selected with a Glan–Taylor CaF_2 prism. Two short-pass spectral filters (FES750, Thorlabs and 3RD-770, Omega Optical) were placed before the entrance of the spectrometer (Shamrock 303i, Andor Technologies). The SF signal was spectrally dispersed onto an intensified CCD camera (i-Star DH742, Andor Technologies). The intensifier was triggered by the laser system with a gate time of 8 ns. The acquisition time of a single spectrum was 300 s. The presented SF spectra in this study are plotted as a function of IR wavenumber. The y-axis units of all graphs labeled with I_{SF} represent background subtracted data that have been subsequently divided by the VIS and IR input energies (measured before the sample) and acquisition time. Graphs labeled I_{SF}/I_{IR} represent data that have been divided by a normalized IR pulse.

Results and discussion

We compare SF scattering experiments to SFG performed in reflection mode using the same sample. This is followed by scattering experiments at different scattering angles, and an experiment aimed at quantifying to which extent transmission

SFG in combination with linear light scattering can interfere with SFS.

Comparison of the droplet–D_2O solution interface and CaF_2–D_2O solution interface

SDS adsorbs on both the droplet surface and the CaF_2–D_2O interface.[59] In the following experiment we have made solutions of droplets containing 1 vol% oil and 8 mM SDS. We then introduced the solution into a sample cell with a 200 μm path length. The beam overlap was first centered on the surface of the CaF_2–solution interface. The phase-matched reflected SFG signal was detected in the reflected direction at $\theta = 300°$. The resulting spectrum (in ssp polarization) is displayed in Fig. 3A. This spectrum is composed of the well-known spectral features of the C–H stretch modes of SDS: the symmetric methylene stretch vibration (d^+, at $\sim$2850 cm^{-1}), the symmetric methyl stretch mode (r^+, at $\sim$2878 cm^{-1}), the Fermi resonance of the CH_3 bending mode overtone with the CH_3 stretch mode (r^{FR+}, at $\sim$2939 cm^{-1}) and the asymmetric methyl stretch mode (r^-, at $\sim$2959 cm^{-1}). The ratio between the symmetric CH_2 and CH_3 stretch modes is the d/r ratio, which is an indicator for chain order. The d/r ratio for our SDS–D_2O–CaF_2 interface is 0.86. The d/r ratio and the spectral shape shown in Fig. 3A are in good agreement with the SFG spectrum from the SDS–D_2O–CaF_2 interface as measured previously by Moore *et al.*[59] The adsorption of SDS on the H_2O–CaF_2 interface was studied earlier, and it was concluded that at low SDS concentrations the CaF_2 surface is positively charged so that a monolayer of SDS is formed at the interface. At concentrations exceeding $\sim$0.3 mM the interfacial charge becomes negative, and the changing SFG spectra were interpreted to originate from a bilayer of SDS molecules.[60] The agreement between our data and the data in ref. 59 suggests that the SDS on the D_2O–CaF_2 interface forms a bilayer with chains that are relatively stretched.

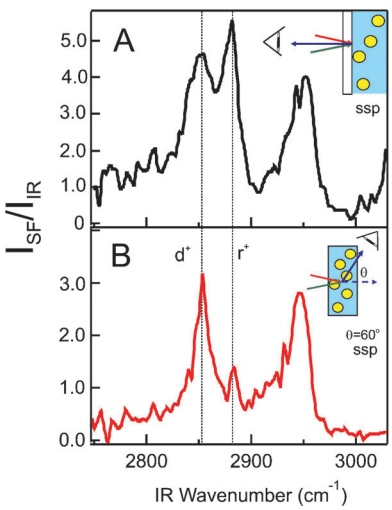

Fig. 3 SFG experiments taken from a 1 vol% dC16-in-D_2O emulsion with 8 mM SDS and 100 nm average droplet radius. The polarization combination was ssp and the sample cell path length was 200 μm. (A) Reflection SFG spectrum recorded from the CaF_2–emulsion interface. (B) SFS spectra taken at a scattering angle of 60°.

Next, we placed the beam overlap in the volume of the bulk phase by translating the sample, and detected at $\theta = 60°$ a scattered SF spectrum. Placing the detection angle at 60° alone is not enough to obtain the SFS signal. The resultant spectrum is displayed in Fig. 3B, and it can be seen that the same vibrational resonances are present. However, the relative intensity of the modes is very different. For the chain conformation a d/r value of $\sim$3.2 is obtained for the ssp spectrum. This indicates that there is a high degree of chain disorder, which corresponds to a projected surface area of $\sim$4.25 nm^2.[28] As discussed in ref. 26 and 28 the SDS forms a monolayer with low density and many chain defects. Therefore, there is a distinct difference in the surface structure of both interfaces, one being comprised of a bilayer, the other consisting of a dilute monolayer. Another point of interest is that the signal to noise ratio for the spectra in Fig. 3A and B is roughly equal.

Different scattering angles

To examine the scattering process further we have taken spectra of an emulsion containing a 1 vol% dC16-in-D_2O emulsion with 8 mM SDS at different scattering angles. We measured spectra at $\theta = 60°$, the angle at which maximum intensity is expected, and at $\theta = 0°$, the phase matched transmitted direction. Measurements were performed in ppp polarization as the signal for this polarization combination is highest. A detailed spectral interpretation can be found in ref. 28. It can be seen from Fig. 4 that an SF spectrum can be recorded at $\theta = 60°$, but not at $\theta = 0°$. This is consistent with scattering theory that predicts a vanishing signal in the forward direction (see Fig. 1C). As the droplets are small and $qR < 1$ it is not very meaningful to measure at other scattering angles for polarization combinations ssp and ppp, because the phase change qR is too small to observe spectral changes.[33]

Quantifying comparative strengths

To identify the comparative strength of transmission SFG with linear scattering and SFS, we have deposited a water insoluble crystalized layer of Poly-(D-Lactic Acid) (PDLA) on the solution side of the CaF_2 window. The film had a thickness of $\sim$1 μm (see ref. 61 for the procedure of film preparation) and the crystalline structure belongs to the $P2_12_12_1$ space group, so that a bulk $\chi^{(2)}$ signal occurs at polarization combination spp. We then measured: (A) the signal in the phase-matched

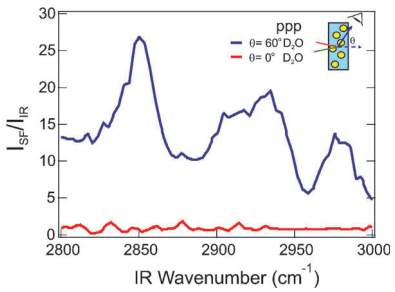

Fig. 4 SFS spectra taken at a scattering angle θ of 60° (top trace) and at 0° (bottom trace), which corresponds to the phase matched direction. The data were taken from a 1 vol% dC16-in-D_2O emulsion with 8 mM SDS and 105 nm average droplet radius. The polarization combination was ppp and the sample cell path length was 100 μm.

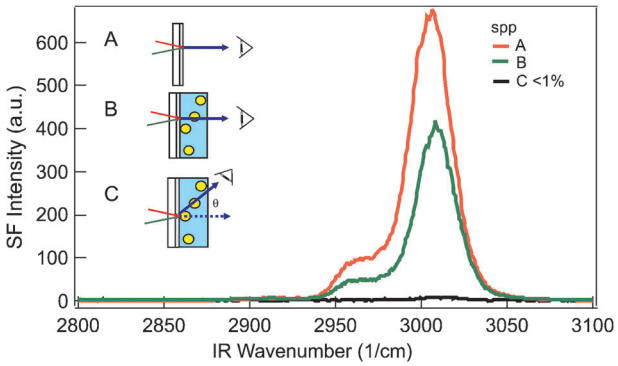

Fig. 5 SF spectra recorded from a sample cell with a crystalline PDLA film on top of the CaF_2 entrance window. The spectra display the bulk window signal in phase matched transmission (A, top trace), the bulk window signal in the same direction but transmitted through an emulsion sample (B, middle trace) and the signal that can be detected at a scattering angle of $\theta = 60^\circ$ (C, lower trace). The emulsion consisted of a 1 vol% dC16-in-D_2O emulsion with 8 mM SDS with a 100 nm average droplet radius. The polarization combination was spp and the sample cell path length was 150 μm.

transmission direction from the bare polymer coated window, (B) the signal in transmission in the phase-matched $\theta = 0^\circ$ direction, with a droplet sample present in the sample cell, and (C) the signal at $\theta = 60^\circ$, with an emulsion sample present in the sample cell. The cartoons in Fig. 5 illustrate these different experiments. This experiment serves to quantify the comparative strength of light scattered from bulk allowed phase-matched transmitted SFG photons and the SFS photons generated in solution.

The spectra in Fig. 5 show that $<1\%$ of the bulk PDLA signal reaches the detector at $\theta = 60^\circ$. In a scattering experiment aimed at detecting photons generated at the droplet or particle surface, this number decreases further because the overlap volume of the IR, the VIS and the detected SF beam must be placed in the bulk phase. With this information we can estimate under which conditions transmitted SF photons may not originate from the droplet surfaces.

As the scattered SF signal and the reflected window signal shown in Fig. 3 are roughly of equal strength it can be concluded that SFG photons generated from the wall of the sample cell do not influence the outcome of the measurement, because 0.1% of the window signal is well below the detection limit of our setup. However, it can become an issue if one performs experiments at scattering angles close to the forward direction using particles of a small size so that the SF scattering cross-section becomes very low (see Fig. 1C). For scattering angles in the range $-10 < \theta < 10$ care needs to be taken to determine whether the SF photons originate from the droplets, as the SF scattering intensity becomes very small, while the linear scattering becomes maximum. If however, a measurement is made for droplets with $R \approx 500$ nm then the scattered signal increases with a significant amount since the signal strongly depends on the radius,[62] so that the scattered intensity might be large still. If the angle of maximum intensity is at angles larger than 30°, for particles with a radius of up to 500 nm, in most experiments particle surfaces can be measured easily.

In the SHS experiment the same mechanism occurs. In such experiments, separating the window contribution from the particle contribution can be done by optimizing the spatial overlap of the exciting beam and the detected signal in combination with appropriate focussing optics. What can be an issue as well in SHS is the generation of Hyper Rayleigh Scattering (HRS), an incoherent second harmonic process that relies on time averaged correlations of the hyperpolarizability tensor.[44] The effect and how to deal with it are described by Schürer *et al.*[21]

Conclusions

We have compared reflection and transmission sum frequency generation from the CaF_2–emulsion interface to SF scattering measurements from the interface of droplets in the same dispersion. It can be seen that signal to noise ratios of SFS and R-SFG are equal, while the spectral shape is very different. In both experiments different chemical environments are probed: DS chains on the CaF_2–D_2O interface form a bilayer while DS chains on the droplet interface form a dilute disorder monolayer. We performed SF scattering measurements on the oil droplet–water interface at different scattering angles. No scattered SF intensity was detected in the phase-matched forward direction. We have quantified the comparative strength of phase-matched SFG and non-phase-matched SFS by using bulk-allowed sum frequency generation from a polymer film in contact with an emulsion.

Our work indicates the feasibility of nonlinear light scattering. Together with recent studies on oil and surfactant structure of nanoscopic droplet interfaces,[26,28] and asymmetry specific leaflet structure of vesicles in water,[32] this work demonstrates the practical use of nonlinear light scattering. In the near future it will be possible to study processes such as the working of ion pumps, the asymmetric distribution of phospholipids across liposome bilayers, the accumulation of sugars on membranes and the transport of molecules across membranes, and cholesterol-induced changes in liposomes and membranes of small cells.

This work is part of the research programme of the Max-Planck Society. We thank the German Science Foundation (grant number 560398) and the European Research Council (Startup grant number 240556).

References

1 R. W. Boyd, *Nonlinear optics*, Academic Press, New York, 1992.
2 Y. R. Shen, *The principles of nonlinear optics*, Wiley, New York, 1984.
3 T. F. Heinz, in *Nonlinear surface electromagnetic phenomena*, ed. H. E. Ponath and G. I. Stegeman, Elsevier, New York, 1991, Chapter Second-order nonlinear optical effects at surfaces and interfaces, p. 353.
4 Y. R. Shen, *Nature*, 1989, **337**, 519.
5 M. B. Raschke and Y. R. Shen, *Curr. Opin. Solid State Mater. Sci.*, 2004, **8**, 343–352.
6 K. B. Eisenthal, *Chem. Rev.*, 1996, **96**, 1343–1360.
7 C. D. Bain, *J. Chem. Soc., Faraday Trans.*, 1995, **91**, 1281–1296.
8 M. J. Shultz, C. Schnitzer, D. Simonelli and S. Baldelli, *Int. Rev. Phys. Chem.*, 2000, **19**, 123–153.
9 G. L. Richmond, *Annu. Rev. Phys. Chem.*, 2001, **52**, 357–389.
10 H. F. Wang, W. Gan, R. Lu, Y. Rao and B. H. Wu, *Int. Rev. Phys. Chem.*, 2005, **24**, 191–256.

11 A. G. Lambert, P. B. Davies and D. J. Neivandt, *Appl. Spectrosc. Rev.*, 2005, **40**, 103–144.
12 S. Roke, *ChemPhysChem*, 2009, **10**, 1380–1388.
13 H. Arnolds and M. Bonn, *Surf. Sci. Rep.*, 2010, **65**, 45–66.
14 H. Wang, E. C. Y. Yan, E. Borguet and K. B. Eisenthal, *Chem. Phys. Lett.*, 1996, **259**, 15–20.
15 K. B. Eisenthal, *Chem. Rev.*, 2006, **106**, 1462–1477.
16 S. Roke, W. G. Roeterdink, J. E. G. J. Wijnhoven, A. V. Petukhov, A. W. Kleyn and M. Bonn, *Phys. Rev. Lett.*, 2003, **91**, 258302.
17 L. Schneider, H. J. Schmid and W. Peukert, *Appl. Phys. B*, 2007, **87**, 333–339.
18 H. F. Wang, T. Troxler, A. G. Yeh and H. L. Dai, *J. Phys. Chem. C*, 2007, **111**, 8708–8715.
19 S. H. Jen and H. L. Dai, *J. Phys. Chem. B*, 2006, **110**, 23000–23003.
20 S. H. Jen, G. Gonella and H. L. Dai, *J. Phys. Chem. A*, 2009, **113**, 4758–4762.
21 B. Schürer, S. Wunderlich, C. Sauerbeck, U. Peschel and W. Peukert, *Phys. Rev. B: Condens. Matter Mater. Phys.*, 2010, **82**, 241404.
22 S. Viarbitskaya, V. Kapshai, P. van der Meulen and T. Hansson, *Phys. Rev. A*, 2010, **81**, 053850.
23 B. Schurer, M. Hoffmann, S. Wunderlich, L. Harnau, U. Peschel, M. Ballauff and W. Peukert, *J. Phys. Chem. C*, 2011, **115**, 18302–18309.
24 S. Wunderlich, B. Schürer, C. Sauerbeck, W. Peukert and U. Peschel, *Phys. Rev. B: Condens. Matter Mater. Phys.*, 2011, **84**, 235403.
25 H. F. Wang, E. C. Y. Yan, Y. Liu and K. B. Eisenthal, *J. Phys. Chem. B*, 1998, **102**, 4446–4450.
26 H. B. de Aguiar, A. G. F. de Beer, M. L. Strader and S. Roke, *J. Am. Chem. Soc.*, 2010, **132**, 2122–2123.
27 H. B. de Aguiar, J.-S. Samson and S. Roke, *Chem. Phys. Lett.*, 2011, **512**, 76–80.
28 H. B. de Aguiar, M. L. Strader, A. G. F. de Beer and S. Roke, *J. Phys. Chem. B*, 2011, **115**, 2970–2978.
29 R. Vacha, S. W. Rick, P. Jungwirth, A. G. F. de Beer, H. B. de Aguiar, J.-S. Samson and S. Roke, *J. Am. Chem. Soc.*, 2011, **133**, 10204–10210.
30 Y. Liu, C. Y. Yan, X. L. Zhao and K. B. Eisenthal, *Langmuir*, 2001, **17**, 2063–2066.
31 J. Liu, M. Subir, K. Nguyen and K. B. Eisenthal, *J. Phys. Chem. B*, 2008, **112**, 15263–15266.
32 M. L. Strader, H. B. de Aguiar, A. G. F. de Beer and S. Roke, *Soft Matter*, 2011, **7**, 4959–4963.
33 A. G. F. de Beer and S. Roke, *J. Chem. Phys.*, 2010, **132**, 234702.
34 A. G. F. de Beer and S. Roke, *Phys. Rev. B: Condens. Matter Mater. Phys.*, 2007, **75**, 245438.
35 B. D. Casson and C. D. Bain, *J. Phys. Chem. B*, 1998, **102**, 7434–7441.
36 K. Lunkenheimer, H.-J. Pergande and H. Krueger, *Rev. Sci. Instrum.*, 1987, **58**, 2313–2318.
37 K. Tsuboi, S. Abe, S. Fukuba, M. Shimojo, M. Tanaka, K. Furuya, K. Fujita and K. Kajikawa, *J. Chem. Phys.*, 2006, **125**, 174703.
38 A. N. Bordenyuk, C. Weeraman, A. Yatawara, H. D. Jayathilake, I. Stiopkin, Y. Liu and A. V. Benderskii, *J. Phys. Chem. C*, 2007, **111**, 8925–8933.
39 G. A. Somorjai and J. Y. Park, *Chem. Soc. Rev.*, 2008, **37**, 2155–2162.
40 R. Campen, A. K. Pymer, S. Nihonyanagi and E. Borguet, *J. Phys. Chem. C*, 2010, **114**, 18465–18473.
41 M. Frederick, J. Achtyl, K. E. Knowles, E. A. Weiss and F. M. Geiger, *J. Am. Chem. Soc.*, 2011, **133**, 7476–7481.
42 C. Humbert, O. Pluchery, E. Lacaze, A. Tadjeddinea and B. Bussona, *Phys. Chem. Chem. Phys.*, 2012, **14**, 280–289.
43 A. G. F. de Beer, R. K. Campen and S. Roke, *Phys. Rev. B: Condens. Matter Mater. Phys.*, 2010, **82**, 235431.
44 J. I. Dadap, H. B. de Aguiar and S. Roke, *J. Chem. Phys.*, 2009, **130**, 214710.
45 S. Jen, H. Dai and G. Gonella, *J. Phys. Chem. C.*, 2010, **114**, 4302–4308.
46 R. K. Chang, J. Ducuing and N. Bloembergen, *Phys. Rev. Lett.*, 1965, **15**, 6–8.
47 R. Superfine, J. Y. Huang and Y. R. Shen, *Opt. Lett.*, 1990, **15**, 1276–1277.
48 S. Nihonyanagi, S. Yamaguchi and T. Tahara, *J. Chem. Phys.*, 2009, **130**, 204704.
49 I. V. Stiopkin, H. D. Jayathilake, A. N. Bordenyuk and A. Benderskii, *JACS*, 2008, **130**, 2271–2275.
50 X. Chen, W. Hua, Z. Huang and H. C. Allen, *J. Am. Chem. Soc.*, 2010, **132**, 11336–11342.
51 R. R. Feng, Y. Guo, R. Lu, L. Valerde and H.-f. Wang, *J. Phys. Chem. A*, 2011, **115**, 6012–6027.
52 R. E. Pool, J. Versluis, E. H. G. Backus and M. Bonn, *J. Phys. Chem. B*, 2011, **115**, 15362–15369.
53 P.-K. Yang and J. Y. Huang, *J. Opt. Soc. Am. B*, 1997, **14**, 2443–2448.
54 P.-K. Yang and J. Y. Huang, *J. Opt. Soc. Am. B*, 2000, **17**, 1216–1221.
55 M. Sovago, E. Vartiainen and M. Bonn, *J. Phys. Chem. C*, 2009, **113**, 6100–6106.
56 A. G. F. de Beer, X. W. H. Chen, Z. Huang, H. C. Allen and S. Roke, *J. Chem. Phys.*, 2011, **135**, 224701.
57 M. Pérez, N. Zambrano, M. Ramirez, E. Tyrode and J. L. Salager, *J. Dispersion Sci. Technol.*, 2002, **23**, 55–63.
58 A. B. Sugiharto, C. M. Johnson, H. B. de Aguiar, L. Aloatti and S. Roke, *Appl. Phys. B: Lasers Opt.*, 2008, **91**, 315–318.
59 F. G. Moore, K. A. Becraft and G. L. Richmond, *Appl. Spectrosc.*, 2002, **56**, 1575–1578.
60 K. A. Becraft, F. G. Moore and G. L. Richmond, *J. Phys. Chem. B*, 2003, **107**, 3675–3678.
61 C. M. Johnson, A. B. Sugiharto and S. Roke, *Chem. Phys. Lett.*, 2007, **449**, 191–195.
62 A. G. F. de Beer and S. Roke, *Phys. Rev. B: Condens. Matter Mater. Phys.*, 2009, **79**, 155420.

